# Tailoring creep behavior via in-situ Ti<sub>3</sub>AIC precipitation in Ti45Al8Nb-0.6C alloy

## Zhe Deng<sup>1,2,\*</sup>,†Pei Liu<sup>1,3</sup>, Wei Wang<sup>1</sup>, Ai-qin Wang<sup>1,3</sup>, and Jing-pei Xie<sup>1,3</sup>, \*,†Zhi-yong Zhang<sup>2</sup>

1.College of Materials Science and Engineering, Henan University of Science and Technology, Luoyang 471023, China
2.State Key Laboratory of Advanced Casting Technologies, Shenyang 110022, China
3.Provincial and Ministerial Co-construction of Collaborative Innovation Center for Non-ferrous Metal New

Materials and Advanced Processing Technology, Luoyang 471023, China

\* Corresponding authors. E-mail: liupei@haust.edu.cn (Pei Liu), ustbamm2011@126.com (Zhiyong Zhang)

† These authors contributed equally to this work.

**Abstract:** In this study, Ti45Al8Nb-0.6C alloy was synthesized via vacuum induction melting (VIM), demonstrating a homogeneous microstructure consisting of ( $\gamma$ -TiAl +  $\alpha_2$ -Ti<sub>3</sub>Al) lamellae, B2 phase, and blocky  $\gamma$  phase, where the B2 phase alternates with the blocky  $\gamma$  phase. High-temperature creep tests show that this material has excellent creep properties, and the creep life of Ti45Al8Nb-0.6C alloy is 144 h at 800 °C/200 MPa. Fracture surface analysis reveals a typical ductile-brittle mixed fracture mode characterized by cleavage steps, river patterns, and shallow dimples, with the main crack propagating perpendicular to the loading axis. Microstructural investigations after deformation show significant formation of the B2 phase and deformation twins, along with microstructural degradation. Notably, coarsened lamellar interfaces contain abundant stacking faults. During high-temperature creep, extensive dynamic recrystallization occurs, generating numerous fine recrystallized grains. The Ti<sub>3</sub>AlC phases play a crucial dual role in strengthening: firstly, they act as effective barriers to dislocation motion; secondly, they develop unique defect configurations, including high-density dislocations and ladder-like stacking faults during deformation. These distinctive microstructural evolutions synergistically contribute to the enhanced creep performance of the alloy system.

Keywords: High Nb-TiAl; Microstructure; Creep properties; Deformation mechanism

### 1 Introduction

TiAl-based intermetallic alloys have emerged as promising lightweight structural materials for aerospace applications due to their exceptional combination of high specific strength, superior oxidation resistance, and excellent high-temperature mechanical properties<sup>[1-4]</sup>. A significant milestone in commercialization was achieved with the successful implementation of Ti-48Al-2Cr-2Nb alloy in GEnx<sup>TM</sup> engine low-pressure turbine (LPT) blades, demonstrating their engineering viability for critical rotating components<sup>[5]</sup>. The growing demand for next-generation aeroengines with higher thrust-to-weight ratios, extended service life, and improved fuel efficiency has driven intensive research on developing advanced TiAl alloys with enhanced high-temperature capabilities [6]. However, broader applications of these alloys remain constrained by their limited high-temperature strength

and creep resistance under extreme service conditions<sup>[7]</sup>. Recent advances in microstructure engineering have revealed that near-lamellar microstructures exhibit particularly outstanding high-temperature strength and creep performance<sup>[8-10]</sup>. These specially designed microstructures maintain adequate ductility while effectively impeding dislocation motion and grain boundary sliding at elevated temperatures, offering new opportunities for developing next-generation high-performance TiAl alloys.

Alloying has been widely recognized as an effective strategy for enhancing the properties of TiAl-based alloys [11-14]. Zhou et al. [15] employed ultrasonic-assisted vacuum arc remelting (VAR) to develop Ti-46Al-2.6C-xNb (x=0-4 at.%) alloys, demonstrating that increasing Nb content from 0 to 4 at.% significantly improved the ultimate tensile strength from 2074 MPa to 2474 MPa while simultaneously increasing the fracture strain from

23% to 28%. In a complementary study, Wang et al.<sup>[16]</sup> successfully fabricated Ti-45Al-8Nb alloy using arc-directed energy deposition (DED), revealing that Nb addition not only effectively reduced internal defects but also substantially enhanced mechanical properties through combined solid solution strengthening, grain refinement, and dislocation strengthening effects when compared with binary Ti-45Al alloy. These findings collectively highlight the crucial role of Nb alloying in optimizing both the processing characteristics and mechanical performance of TiAl alloys.

Although Nb is an effective β-stabilizing element in TiAl alloys, excessive addition can promote the formation of brittle B2 phase, leading to reduced ductility [17-19]. Recent studies<sup>[20,21]</sup> have shown that this detrimental effect can be counteracted by incorporating α-stabilizing elements such as carbon. Beyond compensating for the negative impact of β-stabilizers, carbon addition independently enhances TiAl alloy performance through multiple mechanisms<sup>[22]</sup>. Carbon exhibits limited solid solubility in TiAl alloys, and when its content exceeds ~0.5 at.%, it preferentially forms Ti2AlC (H-phase) and Ti<sub>3</sub>AlC (P-phase) phases [23,24]. Li et al. [25] investigated this systematically phenomenon Ti-43Al-6Nb-1Mo-1Cr-xC (x=0-1.0 at.%) alloys prepared by induction skull melting (ISM). Advanced TEM and HRTEM characterization revealed that P-Ti<sub>3</sub>AlC phases maintain a coherent interface with the γ-matrix, facilitating stress transfer while minimizing interface cracking. These precipitates were found to enhance plastic deformation capability by promoting dislocation glide and mechanical twinning, ultimately leading to improved strength and ductility in high-Nb TiAl alloys.

systematically investigates study optimization mechanism of graphite additives on the mechanical properties of high Nb-TiAl alloy. We successfully developed a Ti45Al8Nb-0.6C alloy prepared via vacuum induction melting (VIM) technology and conducted high-temperature creep performance tests on it. The incorporation of graphite powder facilitates the in-situ formation of carbide reinforcements. We in-depth characterization conducted an microstructural evolution of TiAl alloys before and after deformation. By integrating high-temperature creep performance testing and fracture morphology analysis, this study elucidated the interfacial coordinated deformation mechanism between the carbide reinforcement phases and the matrix and identified the primary strengthening and toughening mechanisms.

#### 2 Experimental section

The master ingot was initially fabricated using vacuum

induction melting (VIM). To achieve microstructural uniformity, the ingot underwent three successive remelting cycles before the test specimens were extracted. Subsequently, test samples were taken from predetermined locations of the homogenized ingot for material characterization. High-purity starting materials were employed, including titanium sponge aluminum rods (99.99%), (99.7% purity). aluminum-niobium master alloy (55 wt% Nb content), and graphite powder (99.98%). The melting process was carried out under a high-purity argon protective atmosphere, which was introduced when the base vacuum level dropped below 5×10<sup>-4</sup> Pa. The resulting ingot had a diameter of 150 mm and a height of 80 mm.

Microstructural characterization was performed using field emission scanning electron microscopy (FE-SEM, Hitachi SU8010) to analyze the deformed structures. For nanoscale investigation, transmission electron microscopy (TEM, FEI Tecnai G2 F30) was employed with bright-field imaging, energy-dispersive X-ray spectroscopy (EDS), and selected-area electron diffraction (SAED) techniques. Metallographic specimens were mechanically ground to #2000 grit, polished, and chemically etched using Kroll's reagent (5 vol% HF + 10 vol% HNO<sub>3</sub> + 85 vol% H<sub>2</sub>O). TEM samples were prepared by wire-electrode cutting, mechanically thinned to below 50 μm, and subsequently electropolished using a twin-jet system. Creep tests were conducted on a universal testing machine under constant conditions of 800 °C and 200 MPa until specimen failure. To ensure temperature stability, three thermocouples were strategically positioned along the upper, middle, and lower sections of the specimen for continuous temperature monitoring, maintaining the experimental temperature within acceptable error limits throughout testing.

## 3 Results and discussion

## 3.1 Microstructure of Ti45Al8Nb-0.6C alloy

The microstructure analysis of Figs. 1a-d shows that the Ti45Al8Nb-0.6C alloy has a uniform lamellar structure, which mainly consists of  $(\gamma\text{-TiAl} + \alpha 2\text{-Ti3Al})$  lamellar organization, while the B2 phase and a small amount of  $\gamma$  phase are distributed at the grain boundaries (Fig. 1e). This special phase distribution characteristic is mainly closely related to the alloy composition and solidification process. Nb, as a strong  $\beta$ -phase stabilizing element, can inhibit the formation of  $\alpha$ -phase during the solidification process of the alloy and induce the ordering transformation of the high-temperature  $\beta$ -phase during cooling, which ultimately results in the formation of the B2-phase at room temperature. In addition, the addition

of C further changes the solidification path of the alloy and promotes the phase equilibrium in the region of high Al content, resulting in the formation of a  $(B2+\gamma)$  mixed-phase structure at the grain boundaries.

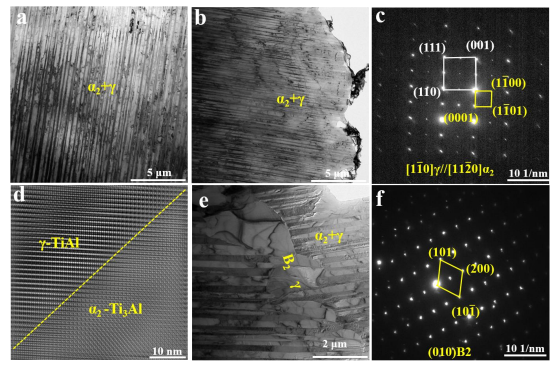


Fig. 1 Microstructure characterization of Ti45Al8Nb-0.6C alloy.

### 3.2 Creep behavior of Ti45Al8Nb-0.6C alloy

Fig. 2a presents the strain-time curve of the Ti45Al8Nb-0.6C alloy under creep conditions of 800 °C/200 MPa, with the red line indicating the corresponding property values. Specifically, the composite exhibited a creep lifetime of 144 hours and a steady-state creep rate of 6.4×10<sup>-8</sup> s<sup>-1</sup> under these testing conditions. A comprehensive comparison of performance between the developed creep Ti45Al8Nb-0.6C alloy and various other TiAl alloys/composites [26-34] is illustrated in Fig. 2b. The comparative analysis clearly demonstrates the superior creep resistance of Ti45Al8Nb-0.6C alloy over other TiAl-based remarkable enhancement in creep performance can be primarily attributed to the strategic incorporation of the carbon element.

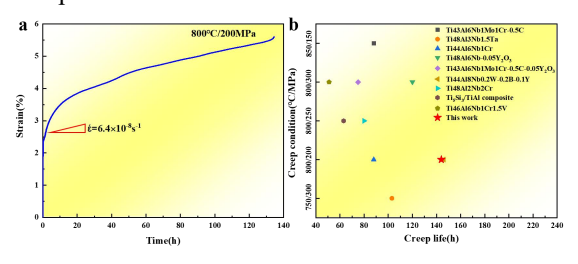


Fig. 2 The analysis of high-temperature creep properties for Ti45Al8Nb-0.6C alloy at 800 ℃. a Creep properties of Ti45Al8Nb-0.6C alloy tested at 800 ℃ under 200MPa. b Comparison of creep properties of Ti45Al8Nb-0.6C alloy with other reported TiAl alloys or composites.

Fig. 3 presents TEM micrographs of the matrix and B2 phase in Ti45Al8Nb-0.6C alloy after creep deformation at 800 °C. As shown in Fig. 3a, irregularly shaped B2 phases are distributed along the  $(\gamma+\alpha_2)$  lamellar matrix, while dislocations are uniformly dispersed within the  $\gamma$ -phase grains. Figs. 3b–c reveal extensive deformation twinning within the  $\gamma$  phase, indicating substantial plastic activity. Additionally, Fig. 3d demonstrates the occurrence of bifurcation dissolution

in the α<sub>2</sub> phase. Figs. 3e-f highlight a high density of dislocations in the lamellar matrix, along with pronounced dislocation entanglement. This observation suggests that dislocation slip serves as the primary deformation mechanism within the lamellae. Previous confirmed studies have that high-temperature deformation activates a significant number dislocations<sup>[35]</sup>. The interfacial dislocations observed here originate from mismatch stresses at  $\gamma/\gamma$  or  $\gamma/\alpha_2$  interfaces, where coherent stresses promote their formation to accommodate lattice misfit. Such interfacial dislocations are known to enhance the mechanical properties of composites. Furthermore, Fig. 3e exhibits parallel dislocation lines with relatively low density. This can be attributed to the initial stages of high-temperature tensile deformation, where intense plastic deformation increases dislocation density, thereby improving the material's deformation resistance. As deformation progresses, excessive dislocation accumulation leads to severe entanglement and the eventual formation of dislocation walls.

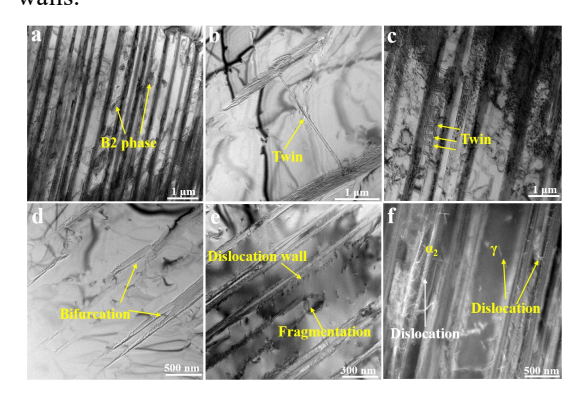


Fig. 3 Deformation characteristics of Ti45Al8Nb-0.6C alloy at 800  $^{\circ}$ C.

Fig. 4 presents a detailed TEM analysis of the microstructural evolution in Ti45Al8Nb-0.6C alloy following creep deformation at 800 °C. As illustrated in Fig. 4a, a significant number of fine recrystallized grains are observed along the grain boundaries of the original lamellar colonies, providing clear evidence for the activation of dynamic recrystallization (DRX) during high-temperature deformation. A closer examination of the yellow-marked region in Fig. 4b reveals that these formed recrystallized grains homogeneous distribution of dislocations, suggesting that plastic deformation continues to occur even after recrystallization. Notably, Fig. 4c shows that some of the recrystallized grains nucleate and grow directly on the lamellar matrix. In addition to recrystallization, Fig. 4d highlights another critical microstructural change—the coarsening of lamellar colonies, which is a typical

phenomenon during prolonged exposure to elevated temperatures. Further high-magnification analysis in Fig. 4e uncovers the presence of extensive stacking faults at the interfaces of the coarsened lamellar structures, indicating that interfacial defects play a crucial role in the deformation and coarsening mechanisms. This observation is further corroborated by the SAED pattern in Fig. 4f, where distinct streaking effects are visible, unambiguously confirming the existence of stacking faults within the lamellar microstructure.

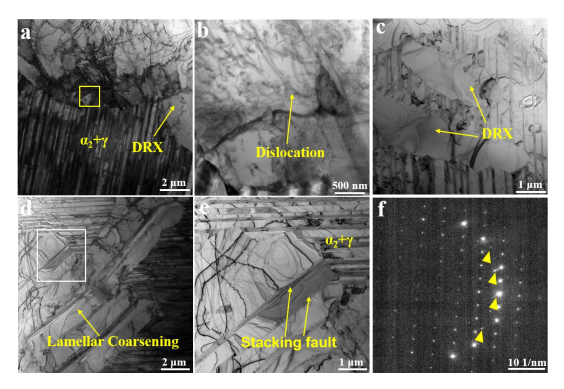


Fig. 5 shows the morphology of Ti3AlC in Ti45Al8Nb-0.6C alloy after creep deformation at 800 °C/200 MPa. As shown in Fig. 5a, the recrystallized grains exhibit a high density of dislocations along with numerous precipitates. Fig. 5b provides a magnified view of the yellow rectangular region marked in Fig. 5a, revealing extensive precipitated phases distributed along these dislocations. Further characterization of the precipitates is presented in Figs. 5c and 5d, which display the SAED pattern and high-resolution transmission electron microscopy (HRTEM) image, respectively. The combined analysis of these figures confirms that the precipitated phase is Ti<sub>3</sub>AlC. Fig. 5e shows the inverse fast Fourier transform (IFFT) image of the Ti<sub>3</sub>AlC phase from Fig. 5d, revealing the presence of dislocations within the precipitate itself. Additionally, Fig. 5f presents the geometric phase analysis (GPA) of Fig. 5d, demonstrating significant stress fluctuations at the interface between the Ti<sub>3</sub>AlC phase and the γ-matrix. The observed precipitates along the dislocation line play a crucial role in hindering dislocation motion, thereby enhancing the alloy's creep resistance and overall mechanical performance. Furthermore, previous studies have demonstrated that elastic interactions between carbon atoms and dislocations lead to the formation of Cottrell atmospheres, which effectively pin dislocation motion<sup>[36]</sup>. To overcome this pinning effect, elevated local stresses are required. Consequently, solute carbon

atoms enhance the alloy's creep resistance by increasing the critical resolved shear stress for dislocation glide.

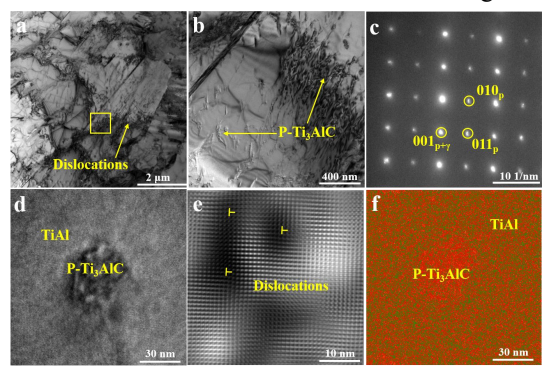


Fig. 5: Deformation characteristics of Ti3AIC in the Ti45Al8Nb-0.6C alloy at 800 ℃. a-b The BF image of the Ti3AIC phase; c The SAED image of the Ti3AIC phase; d The HRTEM image of the Ti3AIC/TiAI phase; e The IFFT image of the Ti3AIC phase; f The GPA image of the Ti3AIC/TiAI phase.

In order to further understand the fracture mechanism of the Ti45Al8Nb-0.6C composite, the microstructures of the fracture surfaces of the Ti45Al8Nb-0.6C composite were analyzed to investigate the root causes and mechanisms of fracture. Fig. 7 shows macro/micro fracture morphology Ti45Al8Nb-0.6C composite. Fig. 7a shows the macroscopic fracture morphology of the composite after high-temperature tensile testing. The fracture surface exhibits typical brittle features with significant topographic variations: a relatively flat central region contrasts with markedly rougher zones at both ends. Figs. 7b-d show the micro-morphological fracture diagrams of the corresponding regions in Fig. 7a, respectively, from which obvious brittle fracture features, such as cleavage facets, tear ridges, and river patterns, can be seen. These fracture morphologies show fine tear edges and zigzag cracks, with no obvious deconvolution surfaces. In addition, some shallow pits with lower density can be observed in Fig. 7b, and this pit morphology is similar to the fracture of along-crystal pits, which is due to the fact that the thermally activated energy is overly involved in the slip and climb process at high temperatures, which helps to alleviate the constraints exerted by localized slip [38]. Some pullout of precipitated phases is also seen in Fig. 7c, which suggests that the second-phase particles bear part of the load during high-temperature stretching and consume energy by shedding during deformation [39]. The above analyses show that the Ti45Al8Nb-0.6C composite can effectively coordinate the deformation process during high-temperature stretching to hinder crack initiation and extension.

Fig. 6a clearly shows an HRTEM image depicting

the path of development of twins in the microstructure observed when external loads are applied to the Ti45Al8Nb-0.6C alloy at 800 °C/200 MPa. Fig. 6b presents the corresponding EDS elemental mapping of the region shown in Fig. 6a, clearly demonstrating the distribution of carbides within the central region of the three twins identified in the microstructure. The spots in Fig. 6c4 can be determined as Ti3AlC phase. Figs. 6c1-c4 show the FFT plots of the twin crystals with the corresponding region of Ti3AlC in Fig. 6a. Fig. 6d shows the IFFT plot of the yellow region in Fig. 6a. Fig. 6e is the IFFT plot of the green region in Fig. 6a. As shown in Fig. 6a, a high density of crystallographic defects is observed at the interface between the two twins. Notably, Twin2 maintains a straight morphology without significant distortion even after intersecting with Twin1. Furthermore, IFFT analysis in Fig. 6d reveals the presence of a distinct atomic disorder zone at the Twin1/Twin2 interface as well as at the interfaces between the twins and the Ti<sub>3</sub>AlC phase. Additionally, a high density of dislocations is distributed in the vicinity of these disordered regions.

As evidenced in Figs. 6a and 6e, a high density of dislocations and stacking faults (SFs) is observed within the Ti<sub>3</sub>AlC, with some SFs exhibiting a distinct step-like configuration. This finding aligns with previous studies by Wang et al. [37], which demonstrated that Ti<sub>3</sub>AlC can be sheared by dislocations, leading to the formation of stacking faults and intersecting stacking configurations. At 800 °C, enhanced local atomic rearrangement mitigates the nearest-neighbor violation around complex stacking faults, thereby promoting the formation of SFs in Ti3AlC. Specifically, the glide of partial dislocations facilitates the propagation of SFs along the {111} planes, which subsequently interact to form intersecting SF configurations. The resulting step-like arrangement may further strengthen the precipitates by acting as effective barriers to dislocation motion, rendering Ti<sub>3</sub>AlC a potent obstacle to dislocation glide at elevated temperatures.

Comprehensive fractographic analysis was performed to investigate the fracture behavior of the Ti45Al8Nb-0.6C alloy, with particular focus on surface morphology characteristics and crack propagation features as demonstrated in Fig. 7. As shown in Figs. 7a-7c, the alloy exhibits typical mixed ductile-brittle fracture characteristics, consisting of cleavage steps, river patterns, and shallow dimples. Particularly, Fig. 7c reveals that these dimples exhibit limited depth, which can be attributed to the hindered formation of B2/γ

interfaces by carbides during creep deformation. Specifically, while dimples preferentially nucleate at B2/γ interfaces under creep conditions, the presence of carbides effectively restricts the development of these interfaces, thereby resulting in the formation of shallow dimples in the Ti45Al8Nb-0.6C alloy. As evidenced in Figs. 7d-7f, the crack propagation path analysis reveals that the primary crack develops perpendicular to the During loading axis. propagation, multiple observed, microstructural evolution features are including microcrack formation, lamellar bending, and crack branching. Specifically, the crack preferentially propagates along  $\alpha_2/\gamma$  interfaces during the initial stage, while significant crack deflection and branching occur in the later stage. These sophisticated crack propagation mechanisms effectively alleviate stress concentration at the crack tip through stress field redistribution, thereby remarkably retarding the final fracture process.

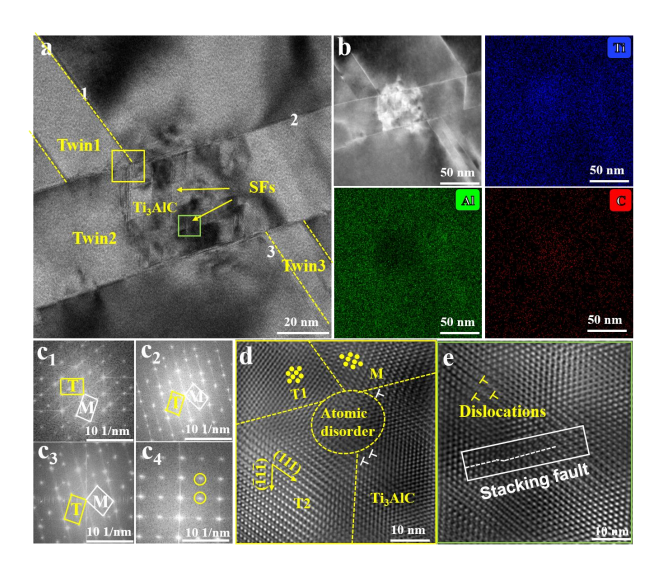


Fig. 6. Deformation characteristics of Ti3AIC in the Ti45Al8Nb-0.6C alloy at 800 °C. a Typical HRTEM image of the deformed Ti3AIC at 800 °C; b Corresponding element distribution in Fig. 6a. c1-c4 The FFT image of HRTEM in Fig. 6a; d The IFFT image of the yellow region in Fig. 6a; e The IFFT image of the green region in Fig. 6a.

Fig. 8 schematically illustrates the creep-induced microstructural evolution in Ti45Al8Nb-0.6C alloy. From the figure, it can be seen that for the Ti45Al8Nb-0.6C alloy, the microstructure consists of (α2+γ) lamellar colonies with B2 phase and blocky γ phase, where the B2 phase alternates with the blocky γ phase. During creep exposure, carbon diffusion facilitates the formation of Ti<sub>3</sub>AlC phase that significantly enhances creep resistance by simultaneously serving as an effective barrier to dislocation motion while inducing unique defect configurations including high-density dislocations and terraced stacking faults (SFs) within the deformed

carbides, which collectively reinforce the Ti3AlC phase at elevated temperatures. Post-deformation characterization reveals substantial dynamic recrystallization and secondary B2 phase precipitation.

Remarkably, crack propagation exhibits preferential orientation perpendicular to the loading axis, with effective stress dissipation achieved through crack deflection and microcrack branching phenomena.

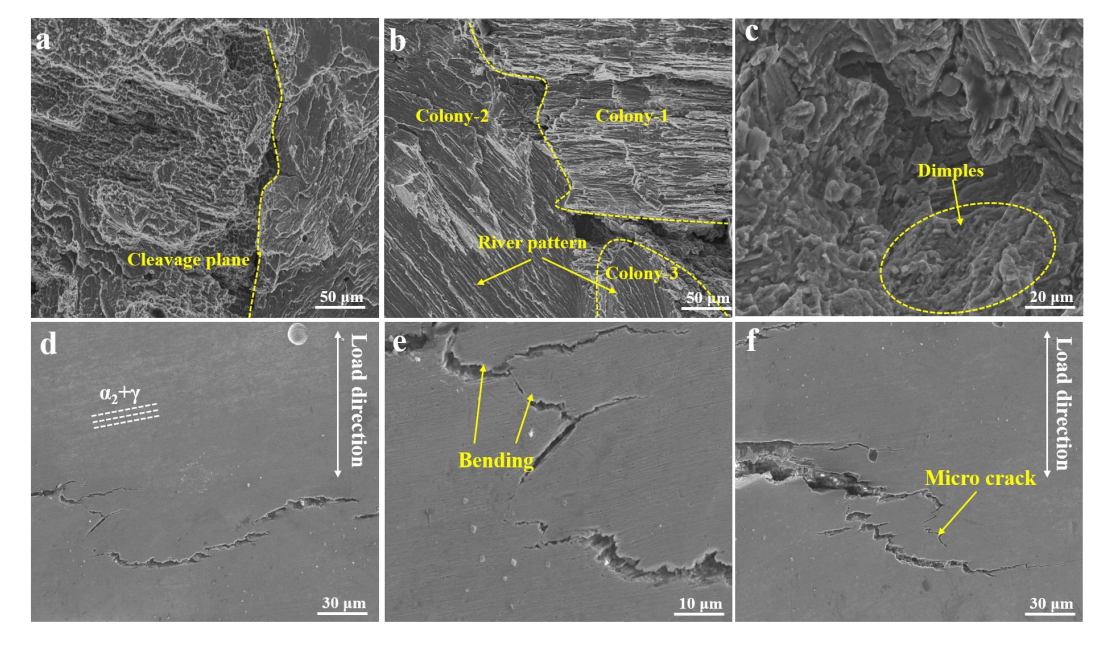


Fig. 7: a-c Fracture morphology of Ti45Al8Nb-0.6C alloy; d-f SEM image of crack extension in Ti45Al8Nb-0.6C alloy.

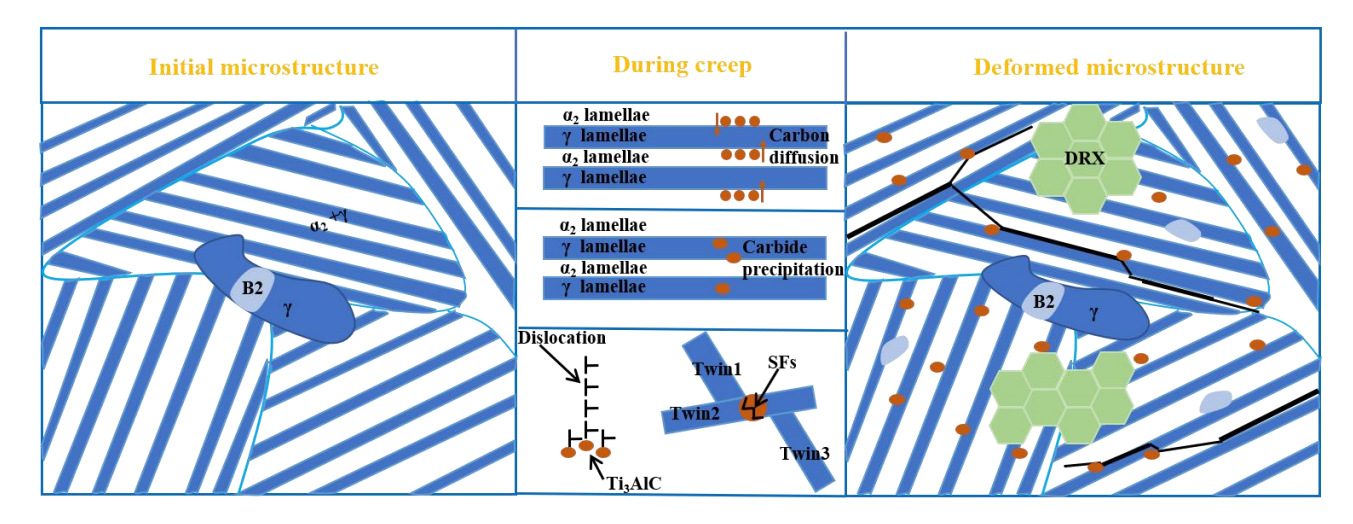


Fig. 8. A schematic diagram illustrating the effect of microstructure evolution on creep resistance of Ti45Al8Nb-0.6C alloy.

#### 4 Conclusions

In this study, Ti45Al8Nb-0.6C composite was fabricated by the VIM method, and its microstructural development was thoroughly investigated. Mechanical property assessments were performed, and the associated deformation mechanisms were analyzed, culminating in the subsequent conclusions:

1. The Ti45Al8Nb-0.6C alloy fabricated via vacuum induction melting exhibits a well-defined microstructure comprising ( $\gamma$ -TiAl +  $\alpha_2$ -Ti<sub>3</sub>Al) lamellae, B2 phase, and blocky  $\gamma$  phase with alternating distribution. This unique microstructure contributes to exceptional creep

resistance, demonstrating a remarkable creep life of 144 h under demanding conditions of 800 °C/200 MPa.

- 2. The Ti45Al8Nb-0.6C alloy shows mixed ductile-brittle fracture features, with cracks growing perpendicular to the loading direction. After deformation, the microstructure changes significantly forming B2 phase, twins, and stacking faults, while also undergoing recrystallization during creep.
- 3. The enhanced creep resistance originates from the effects of Ti<sub>3</sub>AlC phase, which serve dual functions: effectively impeding dislocation motion while developing unique defect configurations including



high-density dislocations and ladder-like stacking faults. These microstructural modifications collectively contribute to the superior high-temperature performance of the alloy system.

#### Acknowledgments

This work was financially supported by the open research fund of State Key Laboratory of Advanced Casting Technologies (Grant No. CAT2023-007), Key Research and Development Program in Henan Province (Grant No. 242102230059) and Natural Science Foundation of Henan Province (Grant No. 252300421326).

#### **Conflicts of interest:**

The authors declare that they have no known competing financial interests or personal relationships that could have appeared to influence the work reported in this paper.

#### References

- [1] S.P. Wang, D.M. Zhu, Z.T. Lu, X.B. Feng, W.J. Li, P.C. Zhai, Y. Chen, G.D. Li, Z.X. Qi, G. Chen, Designing high ductility TiAl alloys based on dislocation nucleation mechanism, Acta. Mater. 292 (2025) 121027.
- [2] Z.Q. Liang, S.L. Xiao, Q.C. Li, X.Y. Li, D.Z. Chi, Y.F. Zheng, L.J. Xu, X. Xue, J. Tian, Y.Y. Chen, Creep behavior and related phase precipitation of a creep-resistant Y2O3-bearing high Nb containing TiAl alloy, Mater. Charact. 198 (2023) 112767.
- [3] Q.B. Wang, S.Z. Zhang, C.J. Zhang, W.G. Zhang, J.R. Yang, D. Duo, D.D. Zhu. The influence of the dynamic softening mechanism of α phase and γ phase on remnant lamellae during hot deformation, J. Alloy. Compd. 872 (2021) 159514.
- [4] H. Ding, X.P. Cui, N.N. Gao, Y. Sun, Y.Y. Zhang, L.J. Huang, L. Geng, Fabrication of (TiB/Ti)-TiAl composites with a controlled laminated architecture and enhanced mechanical properties, J. Mater. Sci. Technol. 62 (2021) 221–233.
- [5] Z. Deng, Z.X. Chen, Y.P. Wang, T.F. Ma, G.J. Li, Q.W. Xing, X.Z. Zhan, D.D. Zhu. In-situ synthesized multi-component particle reinforced TiAl composite with excellent mechanical properties, Mater. Today. Commun. 38 (2024) 108060...
- [6] Z.Q. Liang, S.L. Xiao, H.B. Yu, Q.C. Li, Y.F. Zheng, L.J. Xu, X. Xue, J. Tian, Y.Y. Chen. Enhanced high temperature tensile and creep properties of a β-solidified γ-TiAl alloy with the hybrid addition of C and Y2O3, Intermetallics. 150 (2022) 107698.

- [7] W.G. Yang, M.A. Li, T. Zhou, L. Hu, LX. Shi, S.L. Xiao, Y.Y. Chen, Deformation behavior and dynamic recrystallization mechanism of a novel high Nb containing TiAl alloy in (α+γ) dual-phase field, J. Alloy. Compd. 945 (2023) 169250.
- [8] K.X. Li, H.Z. Fang, J.S. Liang, X.F. Ding, B.H. Zhu, R.R. Chen. Forming Ru containing eutectoid structure serves as the dislocation storage unit at the lamellar colony boundary of TiAl alloy, Acta. Mater. 2024, 120587.
- [9] Z.X. Chen, Z. Deng, Y.P. Wang, T.F. Ma, X.F. Zhang, G.J. Li, Solidification behavior of TiB2-Ti2AlN reinforced TiAl composites with variation Al content, Intermetallics. 178 (2025) 108640.
- [10] D.P. Wang, G. Chen, A.D. Wang, Y.X. Wang, Y.X. Qiao, Z.G. Liu, Z.X. Qi, C.T. Liu, Corrosion behavior of singleand poly-crystalline dual-phase TiAl-Ti3Al alloy in NaCl solution, Int. J. Miner. Metall. Mater, 30 (2023), 689-696.
- [11] Y.Y. Sun, F. Chen, S.W. Qian, N. Wang, J. Ding, H. Chang, X.L. Chen, L. Zhou, Microstructure evolution mechanism of Fe microalloying high Nb–TiAl alloy fabricated by HIP, J. Mater. Res. Technol. 36 (2025) 1273-1282.
- [12] X. Liu, L. Song, A. Stark, U. Lorenz, Z.B. He, J.P. Lin, F. Pyczak, T.B. Zhang, Deformation and phase transformation behaviors of a high Nb-containing TiAl alloy compressed at intermediate temperatures, J. Mater. Sci. Technol, 102 (2022) 89-96.
- [13] X. Guo, Y.J. Zhao, L. Song, D. Lazurenko, T.B. Zhang, Phase transformation mechanisms of hP18 and ωo phases in Zr and Hf containing high Nb-TiAl alloys, J. Alloy. Compd. 1018 (2025) 179214.
- [14] J. Lapin, T. Pelachová, O. Bajana. High temperature deformation behaviour and microstructure of cast in-situ TiAl matrix composite reinforced with carbide particles. J. Alloy. Compd. 797 (2019) 754–765.
- [15] L.Y. Zhou, H.Z. Fang, R.R. Chen, X.K. Yang, X. Xue, Y. Zhang, Y.Q. Su, J.J. Guo, Effects of niobium and ultrasonic action coupling on microstructure evolution and mechanical properties of Ti46Al2.6C alloy. J. Alloy. Compd. 904 (2022) 164048.
- [16] Z. Wang, W. Chen, Z.W. Chen, C.Y. Liu, J.F. Shi, J.Q. Xu, Q. Zhou, Enhanced mechanical properties of TiAl alloy through Nb alloying by Triple-wire arc directed energy deposition, J. Mater. Process. Tech. 339 (2025) 118800.
- [17] D. Wimler, J. Lindemann, T. Kremmer, H. Clemens, S. Mayer, Microstructure and mechanical properties of novel TiAl alloys tailored via phase and precipitate morphology, Intermetallics, 138 (2021) 107316.
- [18] F.M. Qiang, H.C. Kou, B. Tang, L. Song, J.S. Li. Effect of cooling rate on microstructure evolution of Ti-45Al-8.5Nb-0.2W-0.2B-0.02Y alloy during multi-step

- heat treatment, Mater. Charact. 145 (2018) 210-217.
- [19] G. Yang, H.C. Kou, J.R. Yang, J.S. Li, H.Z. Fu, Microstructur e control of Ti-45Al-8.5Nb-(W, B, Y) alloy during the solidification process, Acta. Mater. 112 (2016) 121–131.
- [20] Z.B. Wang, P. Liu, A.Q. Wang, J.P. Xie, B. Hou, Fabrication, microstructure and mechanical properties of TiAl matrix composite reinforced by submicro/nano-Ti2AlC. Mater. Charact. 203 (2023) 113141.
- [21] P. Liu, Z.B. Wang, F. Ye, B. Hou, A.Q. Wang, J.P. Xie, Hierarchically heterogeneous strategy for Ti2AlC/TiAl composite with superior mechanical properties, Compos. B Eng. 273 (2024) 111259.
- [22] J. Lapin, T. Pelachová, O. Bajana. High temperature deformation behaviour and microstructure of cast in-situ TiAl matrix composite reinforced with carbide particles. J Alloys Compd. 797 (2019) 754–765.
- [23] A. Menand, A. Huguet, A. Nérac-Partaix. Interstitial solubility in  $\gamma$  and  $\alpha 2$  phases of TiAl-based alloys. Acta Mater. 44 (1996) 4729–4737.
- [24] C. Scheu, E. Stergar, M. Schober, L. Cha, H. Clemens, A. Bartels, F.-P. Schimansky, A. Cerezo, High carbon solubility in a γ-TiAl based Ti-45Al-5Nb-0.5C alloy and its effect on hardening. Acta Mater. 57 (2009) 1504–1511.
- [25] M.A. Li, S.L. Xiao, L.J. Xu,J. Tian, Y.Y. Chen, Microscale investigation of perovskite-Ti3AlC strengthening and plastic deformation in high niobium containing TiAl alloys, J. Alloy. Compd. 857 (2021) 157563.
- [26] Y. Tian, Q.C. Li, Z.Q. Liang, S.L. Xiao, X.Y. Li, X.C. Wang, L.J. Xu, J. Tian, Y.Y. Chen, Enhanced creep properties and creep-induced microstructure evolution behavior of carbon-doped TiAl alloys, Intermetallics. 181 (2025) 108749.
- [27] Z.B. Zuo, R. Hu, S.Q. Li, Y.J. Lai, Q.X. Wang, X. Luo, Z.H. Qu, T. Chang, J.M. Song, Z.Y. Han, K. Ma, X. Li, A novel Ta-contained TiAl alloy with excellent high temperature performance designed for powder hot isostatic pressing, J. Alloy. Compd. 1008 (2024) 176706.
- [28] Q. Wang, R.R. Chen, Y.H. Yang, J.J. Guo, Y.Q. Su, H.S. Ding, H.Z. Fu, Improvement of the creep lifetimes and microstructural stability of β-solidifying γ-TiAl by cold crucible directional solidification, Intermetallics. 100 (2018) 104-111.

- [29] Y.F. Guo, S.L. Xiao, J. Tian, L.J. Xu, Y.Y. Chen, Creep deformation and rupture behavior of a high Nb containing TiAl alloy reinforced with Y2O3 particles, Mater. Charact. 179 (2021) 111355.
- [30] Z.Q. Liang, S.L. Xiao, H.B. Yu, Q.C. Li, Y.F. Zheng, L.J. Xu, X. Xue, J. Tian, Y.Y. Chen, Enhanced high temperature tensile and creep properties of a β-solidified γ-TiAl alloy with the hybrid addition of C and Y2O3, Intermetallics. 150 (2022) 107698.
- [31] S.G. Tian, Q. Wang, H.C. Yu, H.F. Sun, Q.Y. Li, Microstructure and creep behaviors of a high Nb-TiAl intermetallic compound based alloy, Mater. Sci. Eng. A. 614 (2014) 338-346.
- [32] H.Y. Yue, Z.Q. Liang, F. Zhang, L.J. Fang, P. Chen, L.J. Xu, S.L. Xiao, R.F. Li, Effect of heat treatment on the microstructure and creep properties of Ti–48Al–2Cr–2Nb alloy produced by selective electron beam melting, Mater. Sci. Eng. A. 859 (2022) 144224.
- [33] Y.Y. Zhang, X.P. Cui, X.X. Zhai, J.W. Luo, T.Q. Zhang, Z.Q. Wang, N.N. Gao, H. Ding, J.J. Sun, J.F. Chen, L. Geng, L.J. Huang, Significant enhancement in high temperature performance of TiAl matrix composites by a novel configuration design, Mater. Sci. Eng. A. 889 (2024) 145872.
- [34] Z.Q. Liang, S.L. Xiao, X.Y. Li, D.Z. Chi, Y.F. Zheng, L.J. Xu, X. Xue, J. Tian, Y.Y. Chen, Significant improvement in creep resistance of Ti-46Al-6Nb-1Cr-1.5V alloy via introducing high-density nanotwins, Mater. Sci. Eng. A. 862 (2023) 144485.
- [35] J.H. Liu, Z.M. Wang, P. Li, Z. Zhang, C.G. Zhao, Y. Zhao, Y. Zhang, Y.F. Liang, J.P. Lin, Fabrication of high strength TiAl alloy with nano-lamellar and ultra-fine-grained microstructure by selective electron beam melting, J. Mater. Res. Technol. 35 (2025) 7156–7166.
- [36] M.H. Sun, X. Nie, Z.W. Chen, L.S. Liang, L. Guo, M.J. Wang, C. Zhao, L.X. Li. Improved low-stress thermoplastic forming of TiAl alloys via dislocation behavior under mechanical vibration, J. Alloy. Compd.1022 (2025) 180030
- [37] L. Wang, X.P. Liang, B. Liu, M. Oehring, J. Paul, J. Liu, M. Song, F. Pyczak, Y. Liu, Stacking fault formation in perovskite Ti3AlC carbides in a TiAl based alloy during creep at 800 °C, Scripta Mater. 222 (2023) 115034.